Width-Dependent Dynamics of Warm Filaments: Submesoscale Eddy Generation and Interaction in MITgcm

By

Spencer D. Francis

B.S., Worcester Polytechic Institute, 2023

Thesis

Submitted in partial fulfillment of the requirements for the Degree of

Master of Science in the Department of Physics at Brown University

PROVIDENCE, RHODE ISLAND

May 2025

This thesis by Spencer D Francis is accepted in its present form by the Department of Physics as satisfying the thesis requirement for the degree of Master of Science.

Date 30 April 2025 ______________________

Baylor Fox-Kemper, Advisor

Approved by the Graduate Council

Date ____________ ______________________

Thomas A. Lewis, Dean of the Graduate School

Width-Dependent Dynamics of Warm Filaments: Submesoscale Eddy Generation and Interaction in MITgcm, by Spencer D. Francis, Degree ScM., Brown University, May 2025.

Abstract

This study examines how the width of warm ocean filaments influences the formation and evolution of submesoscale eddies. Using the MITgcm in an idealized, stratified domain, we simulate filaments of varying widths to evaluate their impact on eddy kinetic energy, vertical velocity, and mixed-layer depth. Results show that narrower filaments lead to earlier and more intense central eddy interactions, while wider filaments evolve more slowly but drive deeper and longer-lasting vertical mixing. These trends reveal systematic, width-dependent behaviors in the dynamics and energetics of the system. The findings have implications for understanding oceanic heat and nutrient transport, and emphasize the importance of resolving frontal geometry in both observational and modeling frameworks.

Acknowledgements

Special thanks to Anna Lo Picolo, without whose mentorship this work would not have been possible. I am also grateful to my colaborers at Grace Harbor and within GCMF for their constant support. Thanks to Rebecca. And finally, to Providence.

Contents

List of Figures

List of Tables

1 Introduction

Instabilities that arise at temperature fronts are fundamental to ocean transport. These fronts play a pivotal role in driving ocean circulation on the submesoscale. This study examines the evolution of warm filaments (also called tongues, plumes, or squirts); these structures are characterized by a warm water core bounded by two cold fronts. Our focus is on understanding how variations in filament geometry (in particular, width) affect the development of these instabilities and the formation of interacting frontal eddies. These eddies contribute to vertical mixing and have important implications for the global heat budget.

1.1 Objectives of the Thesis

The primary objective of this thesis is to investigate how width affects the development and intensity of instabilities in warm filaments. Using a high-resolution numerical model, we examine the role of front size relative to the domain in eddy generation. We hypothesize that narrower fronts will induce more rapid and intense overturning, which we characterize through an analysis of the system's energetics.

A particular emphasis is placed on the interactions between eddies generated at the flanking cold fronts. To this end, we focus on the central region of the domain, where these interactions are most likely to converge. We aim to examine the time at which these eddy systems meet in the hopes of supporting future studies of frontal interactions. It is anticipated that narrower filaments, due to their reduced cross-frontal separation, will exhibit earlier interaction events and correspond to more intense eddies.

We assess the impact of eddies on mixing, restratification, and vertical transport. We hypothesize that more intense eddies will correspond to enhanced vertical velocities serving as proxy for stronger vertical exchange. Increased eddy activity, we expect, will also result in shallower mixed-layer depth.

2 Background

Temperature fronts serve as key drivers of submesoscale dynamics. This study focuses on filaments, long narrow flows surrounded by fronts on multiple sides. These features facilitate lateral and vertical transport of heat, momentum, and tracers. Filaments contribute substantially to vertical exchange [LK06]. Warm filaments, in particular, have been identified as significant drivers of upper-ocean mixing [TWR+25]. They also play a role in the offshore transport of dissolved carbon from coastal regions [AS07].

Observational studies have identified such structures in a variety of oceanic context, including strong cold filaments in the Gulf Stream [GMM14] and warm filaments in the Kuroshio Current [SW20]. While cold filaments are often more intense [MCM09] and have received greater attention, warm filaments remain an important yet underexplored phenomenon.

Frontogenesis, the process by which temperature gradients sharpen to create distinct fronts, plays a key role in the behavior and evolution of some filaments. In frontogenetic processes, lateral buoyancy gradients intensify due to straining and convergence. Secondary Circulation and Frontogenetic Tendency (SCFT) diagnostics are commonly employed to quantify such dynamics. Cold filaments typically exhibit positive frontogenetic tendencies, with strong central downwelling. Wind stress can also greatly influence filament evolution, playing an especially key role in shaping secondary circulations [McW17].

2.1 Scale and Eddy Dynamics

As in all fluid-dynamic studies, spatial resolution is a critical determinant of the fidelity of the model. Observational studies have shown that resolution significantly affects the detection and characterization of filament structures. At coarse resolutions, nearby fronts merge, resulting in fewer, elongated features, an imprecision which obscures the underlying dynamics [YF24]. High-resolution data are thus essential for accurately capturing the behavior of filaments.

In situ and remote sensing observations have confirmed that warm filaments can trigger instabilities [HZFL+23], and are frequently associated with mesoscale eddy activity [SW20]. This thesis extends such investigations to the submesoscale regime.

2.2 Role of Submesoscale Eddies in Ocean Circulation

Submesoscale processes, which span spatial scales of 1–10 km and temporal scales of hours to days, have emerged as vital components of upper-ocean dynamics [TT23]. With the advent of advanced computing capabilities and increasingly fine-resolution ocean models, the submesoscale is receiving heightened attention in oceanographic research.

Submesoscale eddies are integral to upper-ocean circulation and play a critical role in the global heat budget. They mediate heat exchange between ocean layers and between latitudes [SWK+18]. Recent studies have shown that submesoscale eddies enhance poleward heat transport, with implications for the redistribution of thermal energy and the dynamics of polar sea ice [ZLQ+23]. As such, understanding their genesis and evolution is essential to accurately modeling large-scale circulation and climate systems.

A variety of mechanisms can drive the formation of submesoscale eddys. Analogous to the filament system, brine rejection at sea-ice edges has been shown to induce overturning circulations and submesoscale eddy generation. Lo Picolo et al. examined such eddy generation as a result of haloclinic fronts. [PHFK24]. As in that case, the overturning process is critically examined in a fixed domain. However, in warm filament systems, the absence of external forcing results in a gradual, internally driven relaxation toward equilibrium.

Flament et al. [FAW85] used infrared satellite imagery to study upwelling filaments off the California coast. Their observations reveal that eddies play a key role in the dissipation of kinetic energy and the formation of the mixed layer. Most relevant to our study, they found that narrower regions within the filament had stronger instabilities and eddies, which motivates a more idealized study isolating filament width.

3 Methods

This study investigates the behavior of warm filament systems through high-resolution numerical simulations using the Massachusetts Institute of Technology General Circulation Model (MITgcm). The simulated domain represents a 160km $\times$ 100km $\times$ 400m section of the upper ocean. Warm filaments of varying widths are initialized in an otherwise steady ocean, and their evolution is tracked over a 15-day period.

3.1 Overview of MITgcm

MITgcm is a versatile numerical model capable of simulating oceanic, atmospheric, and climate processes across a broad range of spatial and temporal scales [MIT24]. It is particularly well-suited for studies of submesoscale dynamics due to its ability to resolve both hydrostatic and non-hydrostatic flows [AHC+04]. For the domain and dynamics considered in this study, we apply the Boussinesq approximation:

$$\nabla \cdot \vec{u} \approx 0$$

allowing the use of MITgcm's hydrostatic solver. At our scale, the effects of diffusion on heat flux are small and can be neglected. This modeling framework is ideal for capturing the evolution of frontal instabilities, overturning circulation, and associated mixing processes.

3.2 Domain Setup

The computational domain spans 160km $\times$ 100km in the horizontal and 400m in the vertical. Grid resolution is 10m in both horizontal directions and 4m in the vertical, resulting in a grid of 1600 $\times$ 1000 $\times$ 100 cells in the zonal (x), meridional (y), and vertical (z) directions, respectively. The simulation progresses over the course of 15 days at intervals of 2 hours.

Periodic boundary conditions are imposed in the horizontal directions to minimize unrepresentative noise along the edges of the domain. The surface is modeled without atmospheric interaction to isolate the internal energetics of the filament system. The lower boundary is stratified to represent a stable deep-ocean background.

3.3 Filament Setup

Initial conditions consist of a warm water filament flanked by two cold fronts, extending vertically to a depth of 100 m. Below this layer, the domain is initialized with stable vertical stratification. To ensure smooth temperature gradients and avoid numerical discontinuities, a stratification profile is applied according to Equation 1:

$$T_{i,j,k} = 10 + dTdz \cdot zC(k) + dTdy \cdot Ly \cdot \frac{1}{2} \cdot \tanh\left(\frac{yC - yM - Wt}{Wt}\right) \cdot \tanh\left(\frac{yC - yM + Wt}{Wt}\right) \cdot e^{-\left(\frac{3 \cdot zC_k}{Ho}\right)^2} \tag{1}$$

where:

$$Ly = \frac{\text{Filament Width}}{2} \cdot dy$$

$$Wt = \frac{\text{Filament Width}}{4} \cdot 1000$$

$$yM = 0; \quad Ho = 400$$

In Equation 1, each hyperbolic tangent represents one front. Their combination, then, makes a filament formed by the two flanking temperature gradients. The resulting temperature field and stratification is shown in Figure 1

Four primary filament widths are tested: reference (40km), wide (60km), narrow (20km), and extra narrow (10km). Initial temperature profiles for each configuration are shown in Figure 2. The fixed meridional width of the domain prevents the expansion of the filament past 60km for for a 15-day experiment, because the overturning will

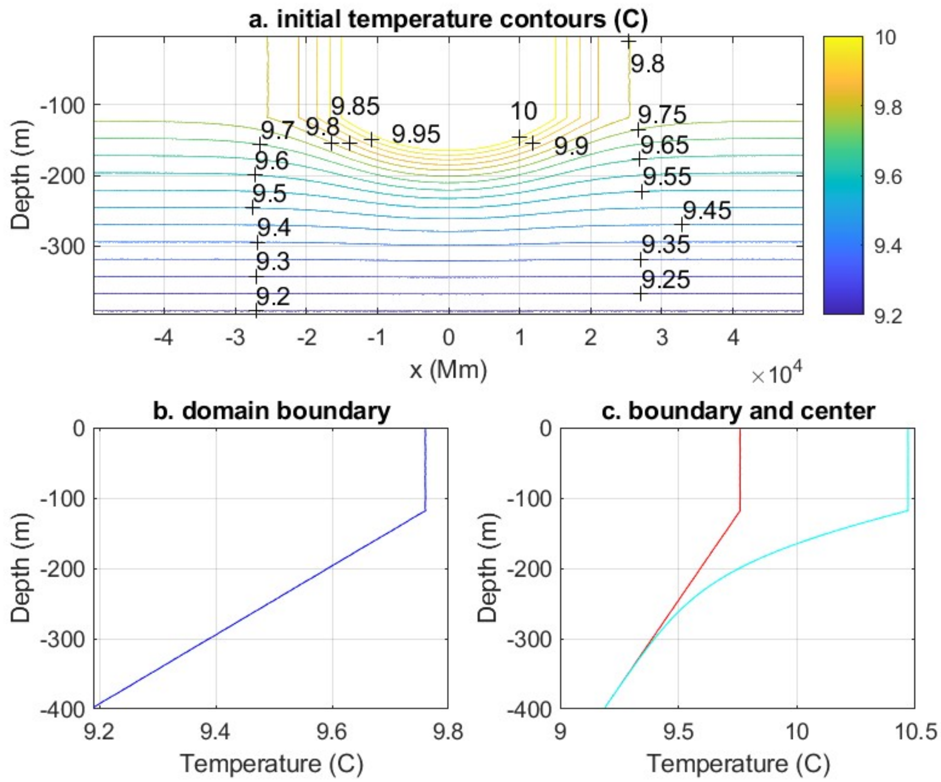

Figure 1: Isothermal structure generated by Equation 1, temperature is given here in degrees Celsius. 1a shows the isothermal contours across the entire domain. 1b shoes the temperature profile at the western boundary of the domain (which is identical to that at the eastern boundary). 1c compares the temperature profile at the boundaries with the profile at the center.

produce interractions at the boundary of the domain.

All simulations are initialized from rest, ensuring that resulting motions stem exclusively from the imposed thermal gradients. The expected evolution involves overturning and mixing that progressively restore stratification.

3.4 Diagnostics and Analysis Methods

To facilitate analysis, model output is averaged along the zonal direction (x-direction), reducing the dimensionality while preserving the essential dynamics. This is justified by the approximate symmetry of the system in the x-dimension.

Key diagnostics include mean kinetic energy (MKE), eddy kinetic energy (EKE), vertical velocity (W), and mixed layer depth (MLD). Eddy kinetic energy and mean

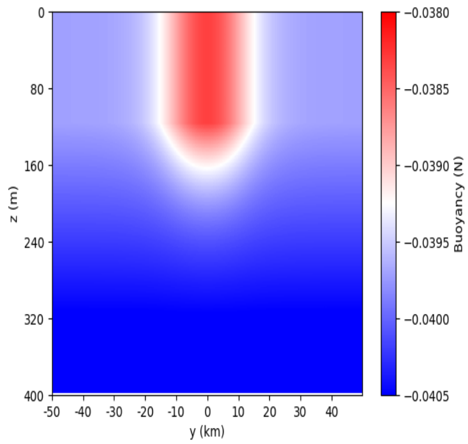

(a) Reference width (40km)

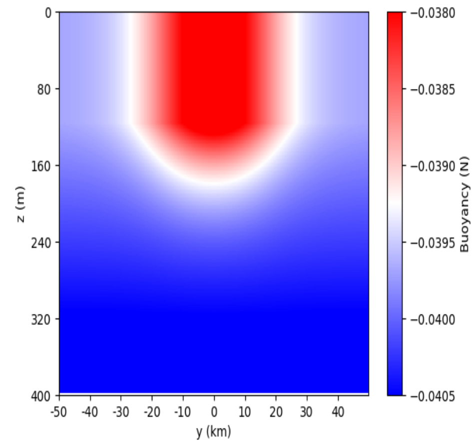

(b) Wide width (80km)

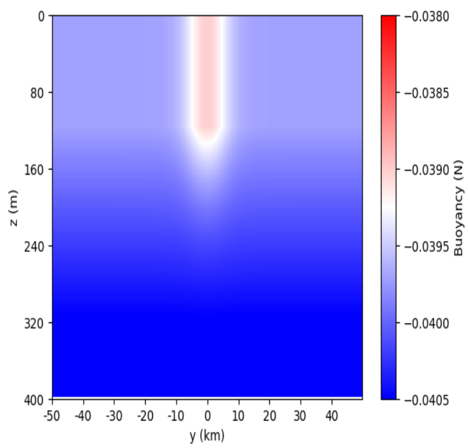

(c) Narrow width (20km)

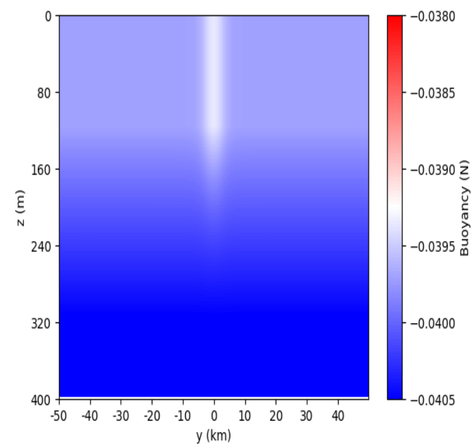

(d) Extra Narrow width (10km)

Figure 2: Initial buoyancy fields for four filament configurations.

kinetic energy are separated using the definition

$$\vec{u} \equiv \overline{u} + u' \tag{2}$$

, where $\overline{u}$ is the mean kinetic energy and u' is the eddy kinetic energy. Buoyancy is used as a proxy for temperature, according to oceanographic convention. These quantities extracted from a NetCDF output file, and parsed using custom-built routines in MATlab and python. The dimensionality reduction in MATlab significantly improves computational efficiency and clarity, particularly given this study's focus on system-scale behavior rather than localized phenomena.

4 Results

When left to evolve without any external forcing or imposed boundary motion, the warm filament gradually overturns and expands laterally, ultimately spreading to occupy a substantial portion of the computational domain. This overturning process serves as a mechanism through which the system restores a state of stable stratification, as denser water masses descend and lighter masses rise in response to initial imbalances. The behavior observed here is consistent across filament widths and is illustrated in Figure 3, which depicts the evolution of the reference filament at three representative snapshots in time. The other filament widths also display same general behavior of overturning and restratification.

The overturning process is not smooth or purely diffusive; instead, it is accompanied by the associated generation of perturbative eddies along the filament's outer boundaries. These eddies form as instabilities at the edges of the filament roll up and intensify, producing vertical exchange and restratification. It is the behavior and interactions of these eddies that constitute the central focus of this study. In particular, we are interested in how the eddies interact, merge, or disperse during critical phases of the experiment, and how these behaviors depend on the initial width of the filament. As shown in Figure 3c, the reference-width filament nearly reaches the domain boundaries at late times, which imposes a practical limitation on both the maximum filament width we can simulate and the maximum duration over which the system can be evolved without interference from boundary effects.

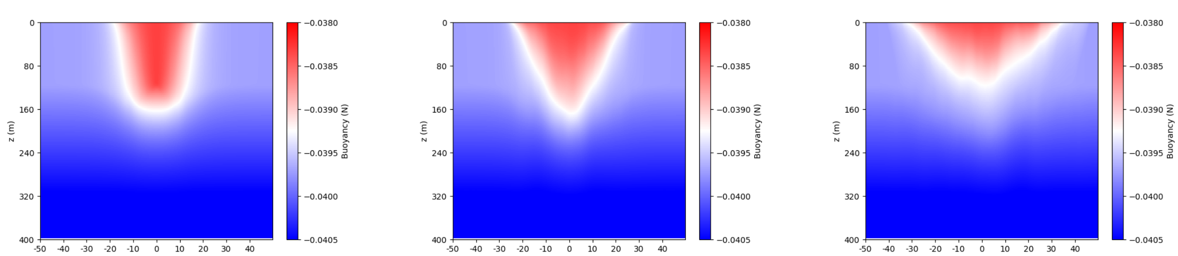

(a) $t = 5$ days (b) $t = 10$ days (c) $t = 15$ days

Figure 3: Snapshots illustrating the temporal evolution of the reference filament (40 km width) at $t = 5$ days (3a), $t = 10$ days (3b), and $t = 15$ days (3c).

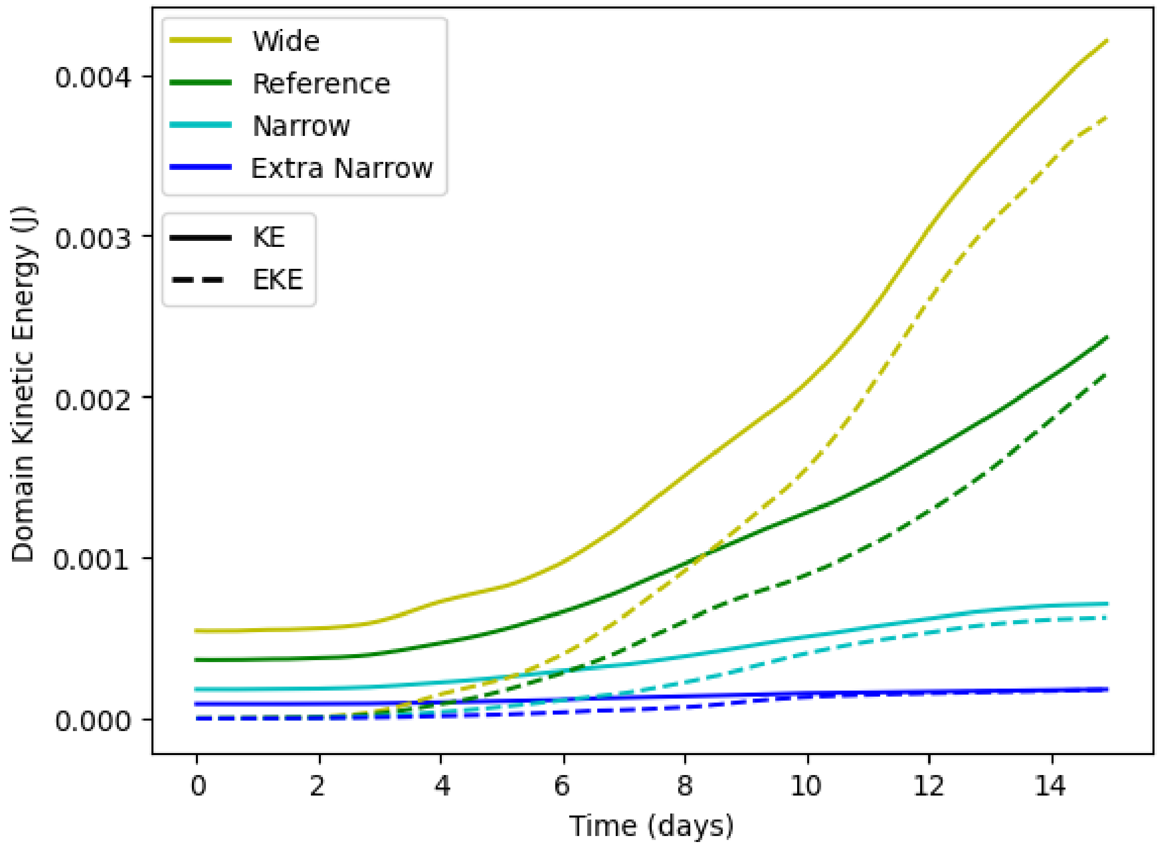

Figure 4: Time series of domain average KE (solid) and EKE (dashed) contained in a grid cell, in Joules. Here, data has been averaged over the zonal and meridional directions. Wider filaments contain a larger amount of kinetic energy because they have a larger volume of water in motion.

Each simulated system begins from rest and undergoes a gradual intensification of kinetic energy as the experiment progresses. This trend is clearly visible in Figure 4, which presents the time series of total kinetic energy (solid lines) and eddy kinetic energy (dashed lines) for each filament width. Notably, wider filaments consistently contain greater amounts of kinetic energy throughout the simulation. This result is physically intuitive: wider filaments encompass larger volumes of water and hence a greater mass of fluid in motion. As a result, these filaments contain more bulk kinetic energy. This observation plays a pivotal role in critically evaluating physical differences between systems with differing initial conditions as we must account for this difference in order to isolate the interesting behaviors of the different geometries.

4.1 Generalized Eddy Strength Across the Domain

To assess the role of eddies in the filament system's energetics, we consider the eddy kinetic energy (EKE) as a proportion of the total kinetic energy (KE). While the unchanged value of EKE itself is useful, it is strongly correlated with the overall energy in the system and therefore with filament width. By normalizing EKE against KE, we obtain a metric that captures eddy activity independently of the scale of motion. This approach allows for more meaningful cross-comparisons between filament systems of different sizes.

Figure 5 shows the normalized EKE over the course of the simulation for all four filament widths. At early times, the similarity in behavior across all systems suggests that initial eddy generation mechanisms operate similarly regardless of width. However, over time, the EKE of the different systems slowly diverge from each other.

We can here begin to identify three regions of interest. An initial period, within the first two or so days, wherein the eddy activity in each filament is similarly small. A second period between 3 and 9 days, where the initial divergences become present. During this period, filament width has a high impact on eddy generation. Finally, at long time scales (around 9 days in our formulation), the filaments converge. We can keep this initial estimate in mind as we proceed with our analysis.

The data in figure 5 provide a broad, global view of the small distinctions between the behavior of the filament systems throughout the entire domain. Importantly, the general global trends are simliar. Our interest lies in the points of divergence between the systems. In order to investigate eddy interactions, and their impact, we must instead turn our focus to a localized area.

4.2 Eddy Interactions

A natural hypothesis, rooted in the symmetry of the initial condition, is that the eddies from either boundary will converge near the domain center. To assess this interaction, we define a region of interest, a five-by-five (500m $\times$ 20m) grid positioned equidistant

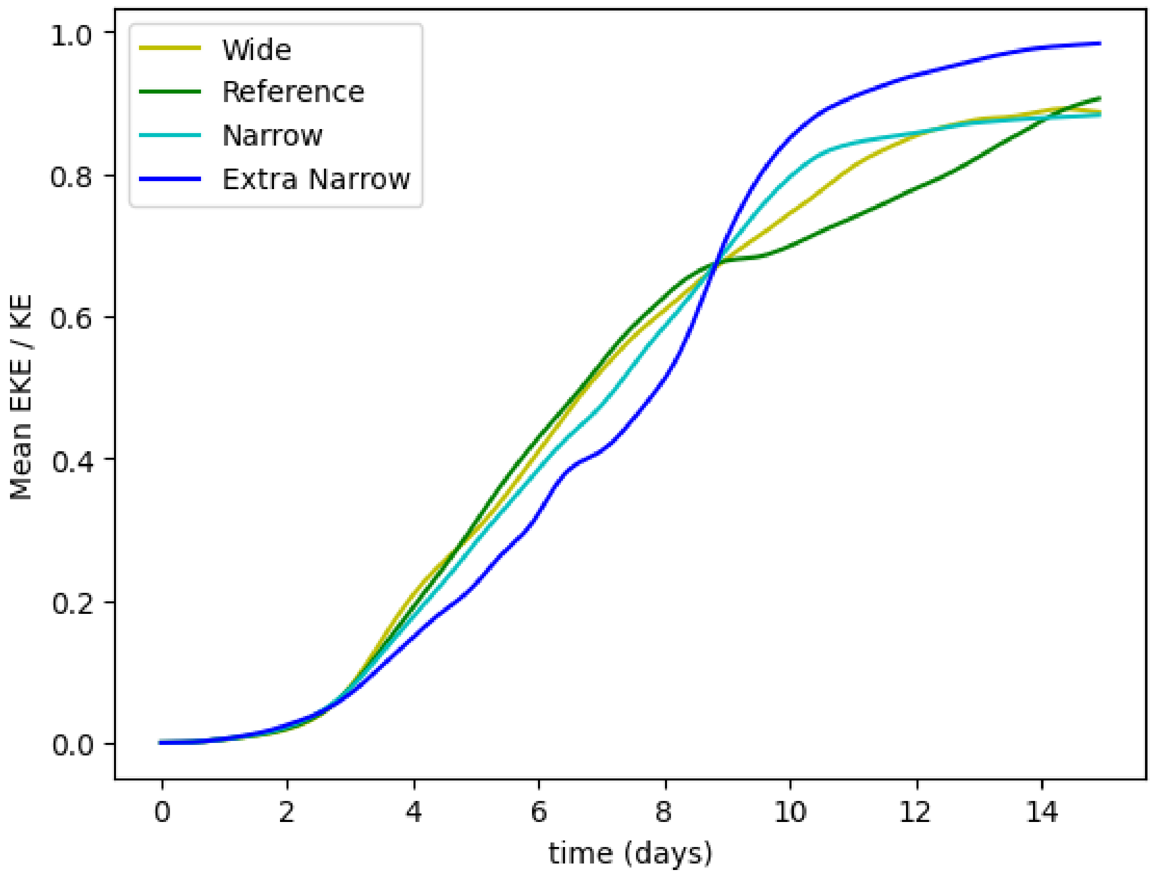

Figure 5: Time series of EKE as a fraction of total KE. Here, a mean is taken in both the zonal and meridional directions. Shows the portion of total kinetic energy which is contained by eddies across the entire domain.

between the northern and southern extremes of the domain. Although this analysis window could be placed on the surface, Figure 6 shows that eddy activity is more concentrated at depth. Eddy Kinetic Energy seeds itself at the foci of an elipse, centered 60m below the surface, equidistant between the two edges of the filament. Importantly, while these foci translate farther apart or closer together depending on the filament width, their depth remains the same across all experiments. Thus, we adopt this depth as our focus for all subsequent central analyses. Measures which follow use an average of the 25 points in the 5×5 central analysis window as a their primary region of interest for localized eddy activity in the center.

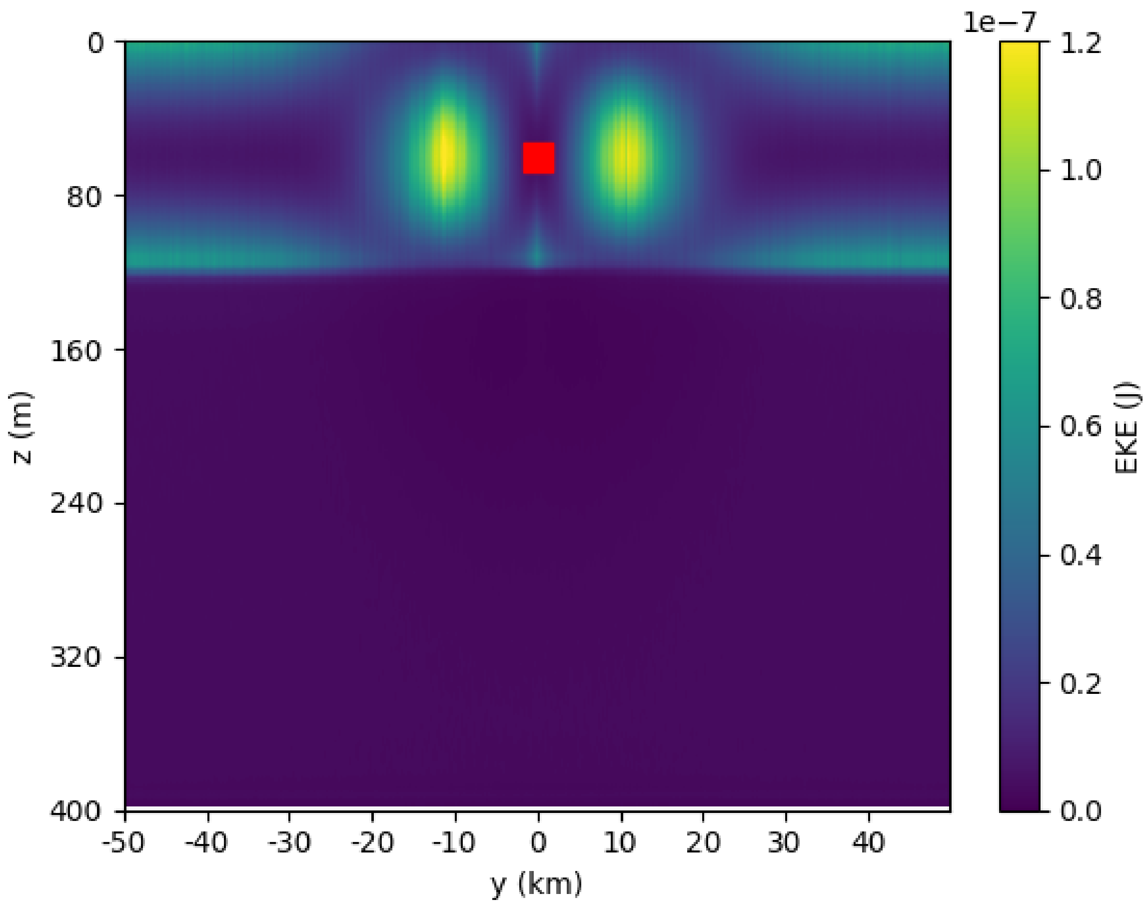

Figure 6: Early-time ($t = 0.08$ days) heatmap of EKE, averaged in the x-direction. Two prominent EKE maxima appear near 60 m depth, guiding the choice of depth for central region analysis. The red square marks the centroid.

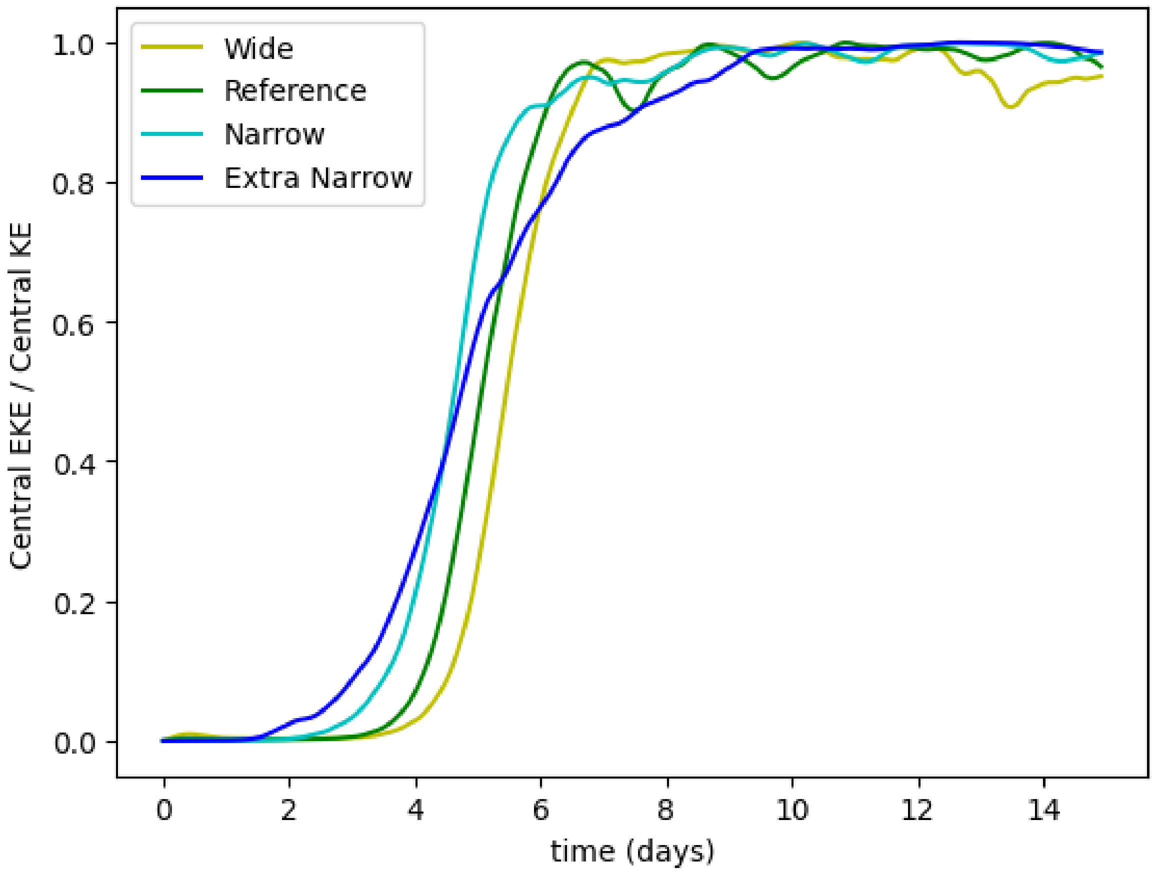

Figure 7: Time series of the EKE-to-KE ratio in the central analysis window. Here, both values (EKE and KE) are localized, providing a measure of the proportion of kinetic activity in the central window which is due to eddies.

4.3 Characterization of Eddy Interactions

Within this central analysis window, we evaluated the ratio of EKE to total KE over time to quantify the emergence and evolution of eddy structures. Figure 7 reveals a sigmoidal pattern in all systems: EKE initially constitutes a negligible fraction of the energy budget, but grows exponentially to dominate dynamics in the center. This growth proceeds more rapidly for narrower filaments, whose curves appear to be shifted left, i.e. backward in time.

To better understand the magnitude and timing of eddy growth, we examine the EKE values in the analysis window. Here, more distinct differences emerge. Figure 8a shows that all systems begin with near-zero central EKE, followed by sharp increases. Importantly, narrower filaments exhibit both earlier and higher peaks in central EKE.

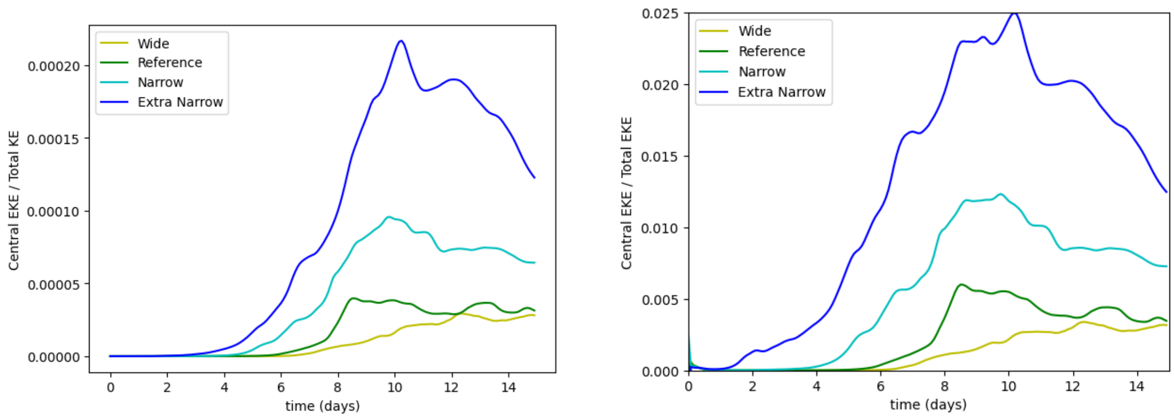

(a) Normalized against domain total KE

(b) Normalized against domain EKE

Figure 8: Comparison of eddy kinetic energy (EKE) time series: normalized against the total kinetic energy (KE) of the domain (left panel, 8a), and normalized against the domain EKE (right panel, 8b). Normalization against KE accounts for broader dynamics, while normalization against EKE measures the concentration of eddies within the central window.

Once again, we see an initial period wherein all filaments behave simlarly. Compare this to the periods noted in Figure 5.

The spatial location of this energy is also of interest. Figure 8b tracks the proportion of EKE within the domain that is contained within the central analysis window. Again, narrower filaments display stronger centralization of eddy energy, with little overlap across systems. Here there is also distinct behavior in the initial period. In Figure 8b, there is no initial period of similarity between the behavior of the filaments. This highlights that in narrower filaments, a disproportionate amount of the total eddy kinetic energy is located within the central analysis window. This pattern is visible form the beginning of the experiment.

To loosely quantify the divergence found in Figure 8a, we define a ”critical time” when central EKE surpasses 0.1% of total KE. Figures 9a and 9b show the crossing points and relationship between filament width and critical time, respectively. This point represents a primative indicator of the transition between period 1 and period 2. The scatter plot in Figure 9b reveals a quadratic trend, indicating systematic variation in eddy onset timing as a function of width.

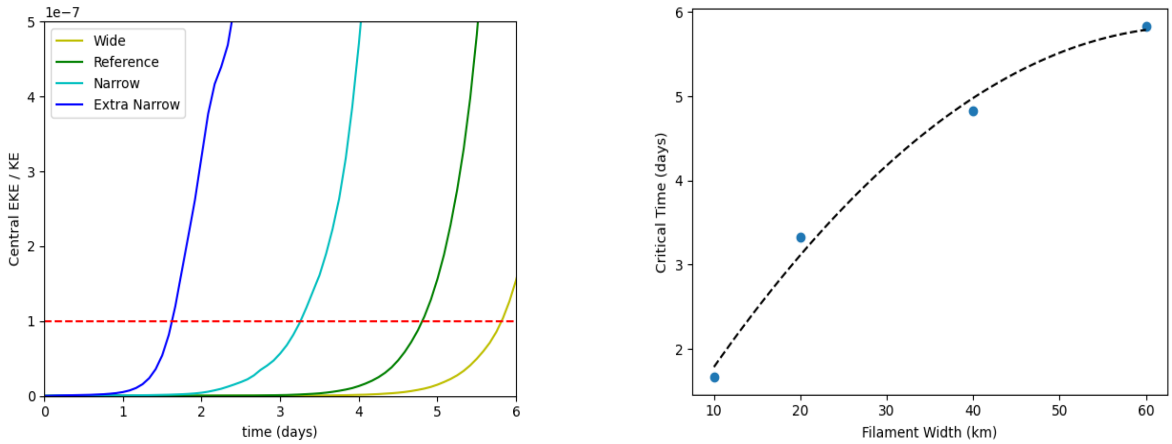

(a) (b)

Figure 9: The scatter plot in 9b shows quadratic fit of critical time as a function of filament width. Critical time is defined in 9a, time series showing when central EKE exceeds a threshold of 0.01% of total KE.

4.4 Characterization of Vertical Transport

In addition to the horizontal dynamics observed in eddy generation and kinetic energy evolution, we turn our attention to vertical transport; beginning specifically with the vertical velocity component W in the central analysis window. Figure 10 shows the time series of vertical velocity at this central location for all four filament widths.

The curves in this plot naturally segment into three distinct temporal regimes, similar to Figure 5. The first regime extends from the initial time to the end of the first day. During this interval, all filament systems exhibit a sharp vertical velocity spike. Early vertical transport so far from the filament edges must be due to overturning, since there is little eddy kinetic energy in the central analysis window at this time. Interestingly, this spike during the overturning-dominated period is strongest for the widest filaments. This suggests that initial overturning in wider filaments is more forceful, possibly due to a stronger initial density gradient and the larger reservoir of potential energy available for conversion to motion.

The second regime spans from the end of day one to a system-dependent time (between 4 and 8 days). During this interval, the vertical velocity undergoes a slower but sustained climb toward a local maximum. Here, the behavior flips; during the eddy-generation period, narrower filaments now exhibit the fastest rates of increase in vertical velocity and reach their respective peaks earlier than the wider experiments. This reversed ordering reflects a transition in dominance from initial, filament-driven overturning to eddy-driven vertical motion.

Finally, the third regime extends from the peak vertical velocity to the end of the simulation. In this late stage, vertical velocity decays its behavior is until dominated by low-amplitude noise, with no clearly discernible ordering between systems. This decay corresponds to the period after major eddy interactions and generations have occurred. The eddies which remain have grown to encompass so much of the domain, the filament widths can no longer be distinguished from each other.

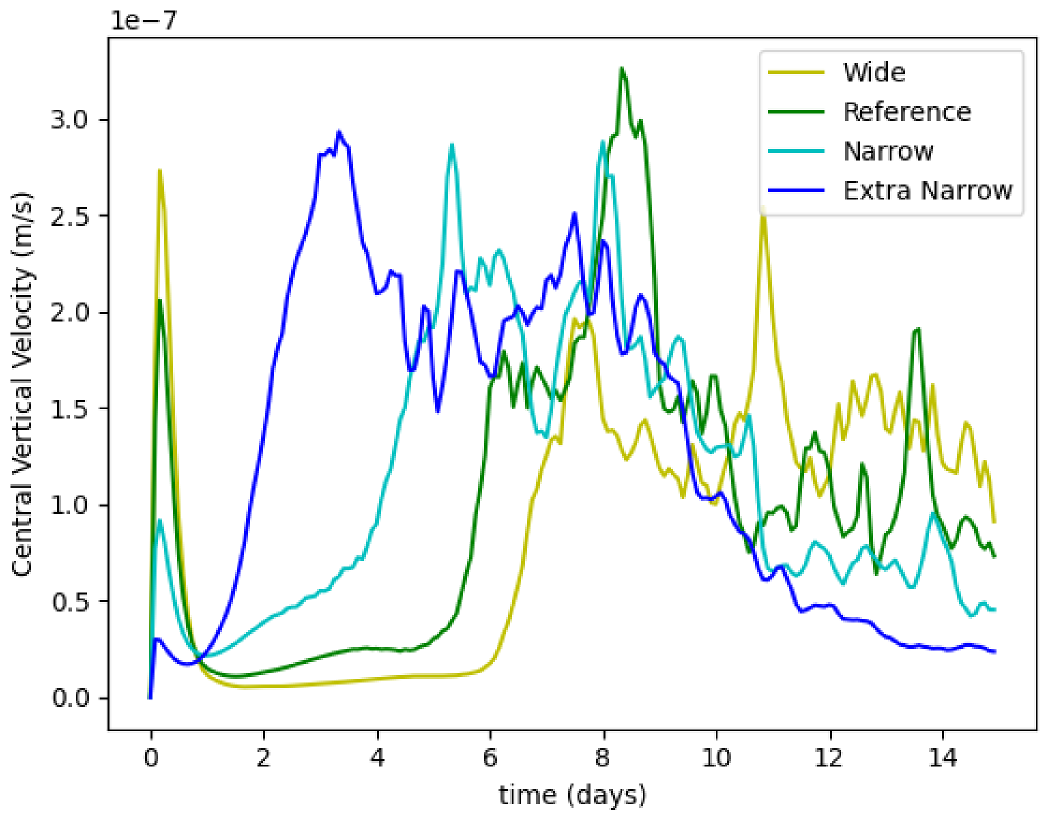

Figure 10: Time series of vertical velocity (W) in the central analysis window for each filament width. Data is averaged over the central analysis window.

4.5 Mixed-Layer Depth as an Indicator of Vertical Mixing

To further evaluate the impact of eddy dynamics on vertical transport processes, we analyze the evolution of mixed-layer depth (MLD), which serves as a proxy for the extent of vertical mixing induced by eddy activity and overturning. Deepening mixed layer indicates the penetration of turbulence into deeper portions of the water column.

Figure 11 presents MLD over the domain in the form of Hovmöller diagrams for three representative filament widths (narrow, reference, and wide). These diagrams reveal a strikingly consistent pattern across all systems. Their most prominent feature is a central spike in mixed-layer depth appears early in the simulation and gradually decays over time. The diagrams have been cropped at the width of the filament in order to highlight this similarity. This spike is localized to the central y-region, consistent with the location of eddy interaction, and slowly dissipates outward in both space and time. Later in the experiment, there also appear regions of deepened MLD along the edges of each filament, but a detailed investigation of this behavior is beyond the scope of this thesis.

Closer inspection of the diagrams reveals that wider filaments generate taller and more persistent central MLD spikes, suggesting stronger and more sustained vertical mixing. Narrower filaments also produce central deepening, but the resulting MLD structures are shallower and decay more quickly. This trend once again reflects the higher initial energy content in wider systems and the more rapid saturation of eddy activity in narrower ones.

While the Hovmöller diagrams provide a spatially resolved view of MLD, we also investigate its time evolution at the center of the domain. Figure 12 shows the time series of central mixed-layer depth for all filament systems.

The results mirror earlier observations. All systems exhibit a rapid deepenning in central MLD near the start of the experiment, followed by a gradual return to a shallower state. This return reflects the restratification caused by eddies. Narrower filaments exhibit this dip earlier, and their maximum MLD values are consistently

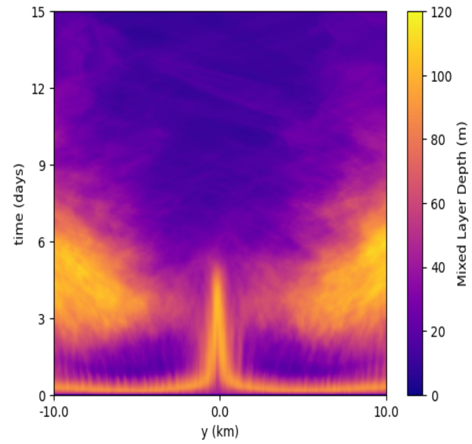

(a) Narrow (20 km)

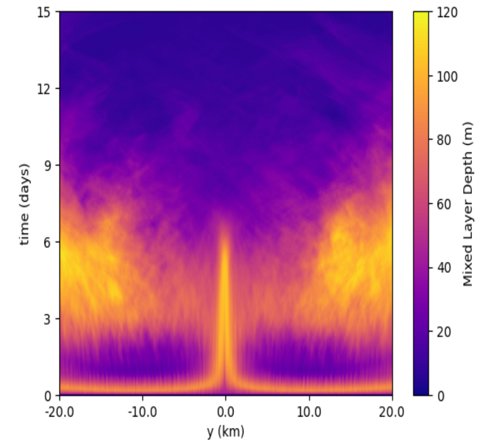

(b) Reference (40 km)

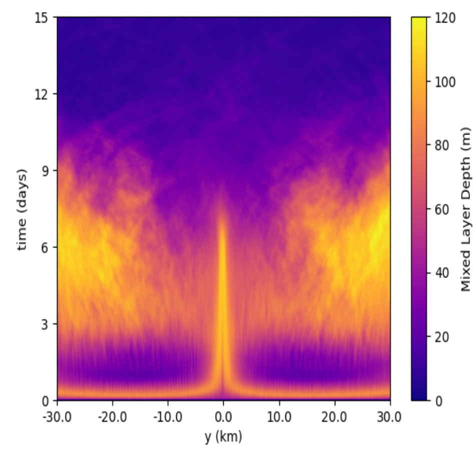

(c) Wide (60 km)

Figure 11: Hovmöller diagrams showing the evolution of mixed-layer depth for three filament widths. Diagrams are averaged in the zonal direction, and have been cropped to only show the filament region in the meridional direction. Central deepening is strongest and most prolonged in wider filaments.

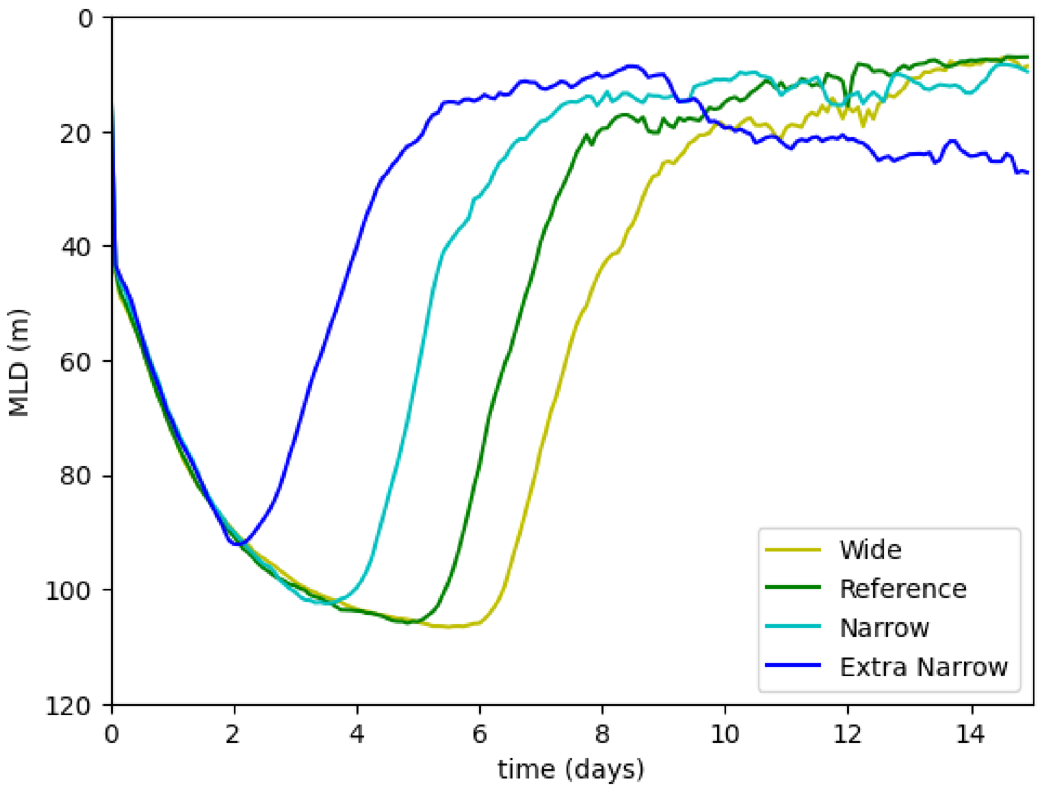

Figure 12: Time series of mixed-layer depth at the center of the domain, for each filament width. Data is averaged over the meridional and zonal directions.

shallower. Conversely, wider filaments experience delayed but more pronounced mixing; this reflects the more pronounced spike in vertical velocities we observe in Figure 10 during the overturning phase. This again highlights a width-dependent critical time for vertical mixing and reinforces the coupling between horizontal eddy evolution and vertical transport processes.

To quantify this analysis, we may examine the time when maximum mixed-layer depth is reached. Figure 13 shows these times. Notice that both the MLD critical times and the EKE critical times (defined in Figure 9) vary quadratically.

Taken together, these observations reveal a consistent and coherent narrative: filament width serves as a control parameter that modulates both the timing and magnitude of dynamical processes across multiple domains of physical behavior, including horizontal eddy generation, vertical transport, and restratification. Systems initiated with narrower filaments evolve more rapidly and saturate earlier, while wider filaments

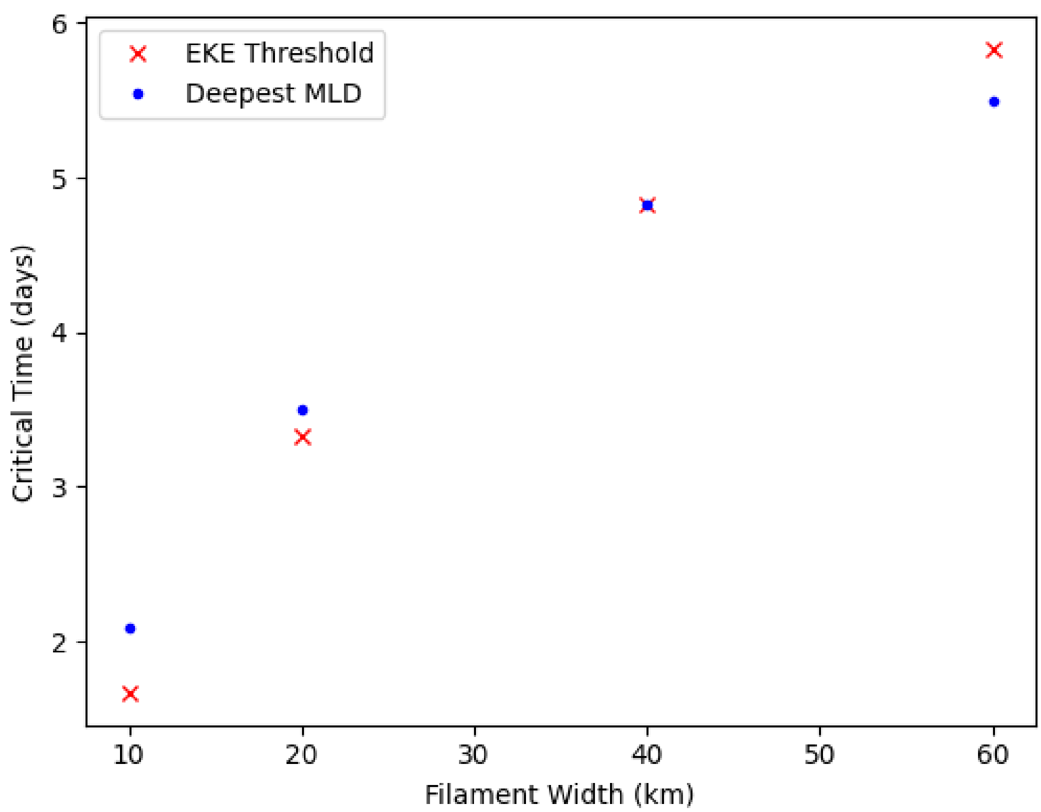

Figure 13: Scatter plot showing the critical times for various filament width. Shown here is critical time defined both with eke threshold (as in Figure 9) maximum mixed-layer depth. Both vary quadratically.

evolve more slowly but generate stronger, longer-lasting dynamical features. The progression of energy from large-scale overturning to localized eddy interaction and eventual dissipation proceeds through clearly identifiable stages, each with hallmarks that differ systematically across filament sizes.

5 Discussion

Across all simulations, the filament width was found to exert two major controls on system evolution: (1) it modulates the strength and timing of central eddy formation and interaction, and (2) it regulates the temporal and vertical extent of mixing processes, especially in the context of mixed-layer development.

5.1 Strength of Eddy Interactions

The results indicate a clear inverse relationship between filament width and the intensity of eddy interactions at the center of the domain. Narrower filaments produce stronger and more rapid surges in eddy kinetic energy relative to the total kinetic energy of the system. This behavior can be understood physically: as the width of the filament decreases, the opposing temperature fronts are brought closer together. This spatial proximity facilitates earlier interactions during the overturning process, leading to a quicker onset of baroclinic instability and a more abrupt burst of energy conversion into eddy activity.

This behavior manifests in both the timing and amplitude of the eddy kinetic energy curves centered in the domain. The narrower filaments not only reach their peak EKE earlier but also exhibit more intense, localized vertical activity. The shorter time scales and larger energy fractions involved underscore the vigorous, albeit short-lived, dynamics of narrow frontal systems.

5.2 Impact of Eddies

In evaluating the physical impact of these eddy interactions, we consider two primary indicators: vertical velocity and mixed-layer depth, both at the center of the filament.

The vertical velocity time series (Figure 10) provides insight into the overturning behavior of each filament. Upon generation, all filaments initiate overturning, reflected in an early spike in vertical velocity. Interestingly, this initial spike is strongest for the wider filaments, consistent with their larger energy reservoirs and deeper initial penetration. However, this trend reverses as the simulation progresses. In the subsequent days, narrower filaments display a steeper and more sustained increase in vertical velocity, indicating a more rapid intensification of circulation caused by the generated eddies. This growth phase is relatively short-lived (typically occurring between days 1 and 8 of the experiment) after which the vertical velocity signatures become noisy and indistinguishable between systems.

A similar trend is observed in the mixed-layer depth. As the filament overturns and eddies emerge, turbulent mixing leads to transient deepening of the mixed layer. Importantly, the deepest mixing occurs early in the experiment, prior to the peak of eddy activity. This confirms that narrower filaments see faster eddy generation and interaction, which leads to a restratification which shallows the MLD.

The spatial distribution of MLD also reveals a central maximum, consistent with the symmetry of the eddy field. Narrower filaments reach their deepest MLD earlier, while wider filaments continue deepening later into the simulation. As with vertical velocity, a period of distinct, width-dependent behavior can be identified outside of which differences between systems decay and the domain enters a more homogenized state.

Taken together, the vertical velocity and mixed-layer depth observations reinforce the conclusion that narrower filaments evolve more rapidly. These systems transition through the overturning-dominated stage and eddy-generating stage faster than wider filaments. While shorter, the eddy generating phase of narrower filaments involves a higher concentration of eddy kinetic energy; in this way, narrower filaments could be characterized as dynamically ”fast and hot.” They initiate intense localized eddy activity that saturates and decays more quickly and leads to shallower but earlier mixing. Wider filaments, in contrast, produce prolonged, gradual impacts on the vertical structure of the domain.

5.3 Observational Implications

The results of this study have direct implications for the interpretation and resolution of observational data. As demonstrated, filament width plays a fundamental role in modulating the evolution of submesoscale processes. Accurately resolving these dynamics requires observational systems with sufficient spatial and temporal granularity.

In our simulations, a horizontal resolution of 100 m was employed, which is fine enough to capture the essential features of frontogenesis, overturning, and eddy development. However, in many real-world scenarios, particularly satellite-based remote sensing, observational data may lack such fine resolution. To detect the early onset of eddy interactions or the detailed evolution of vertical transport processes, comparable resolution (or finer) is required. This suggests that higher-resolution satellite missions or in situ measurements may be necessary to fully capture the rapid dynamics of narrow filaments.

What's more, the differences in timing and magnitude of eddy-related signals such as changes in vertical velocity and the shallowing of the mixed-layer highlight the need for careful sampling. Systems that evolve on time scales of only a few days, as is the case here, may be entirely missed or mischaracterized if observations are not conducted at a high enough frequency.

Thus, our findings underscore the importance of designing observational strategies that are sensitive to the width-dependent characteristics of frontal filaments. Understanding the role of filament width not only informs fundamental energetics but also has broader implications for biogeochemical fluxes, nutrient cycling, and ecosystem responses, all of which are influenced by the intensity and depth of submesoscale processes.

6 Conclusions

In this study, we explored the influence of warm filament width on the energetics of submesoscale oceanic flows, with a particular focus on the formation and evolution of frontal eddies near the central axis of an idealized domain. Using a series of numerical simulations performed with MITgcm, we analyzed how variations in filament width affect eddy kinetic energy, vertical velocity, and mixed-layer depth over time.

Our results reveal two key relationships. First, we identify an inverse relationship between filament width and the relative proportion of eddy kinetic energy from interactions at the center of filaments. Narrower filaments exhibit stronger and more abrupt eddy kinetic energy surges, highlighting the importance of filament geometry in driving intense submesoscale activity. Second, we observe a direct relationship between filament width and the relaxation time of the system. Wider filaments evolve more slowly, sustaining elevated kinetic energy and mixing for longer periods, while narrower filaments transition through their energetic stages more quickly.

These findings contribute to the broader understanding of submesoscale frontal dynamics by characterizing how geometric properties of filaments govern the onset, intensity, and duration of dynamical processes in stratified flows.

6.1 Future Work

Due to the constraints of simulation time and computational resources, the present study adopted a narrow scope, but this focus opens several pathways for future investigation.

One immediate avenue of research would be a formal characterization of the critical time associated with the onset of central eddy interactions. By nondimensionalizing this time scale, future studies could establish a predictive framework for filament evolution based on initial conditions. This includes an analysis of advective and diffusive timescales within the system. Such metrics could also facilitate comparison across numerical models and observational datasets.

Further work could explore the role of domain size, particularly the relationship between filament length and width. In the present study, width was varied while the domain size remained fixed. Adjusting both parameters could yield insight into how confinement, aspect ratio, and boundary proximity shape the simulated dynamics of overturning and eddy generation.

Additionally, the current simulation setup omitted atmospheric interactions in order to isolate the buoyancy-driven response of the system. Future studies could reintroduce surface forcing mechanisms such as wind stress, heat fluxes, or precipitation, all of which are known to affect filament systems. Similarly, exploring the evolution of warm filaments beneath sea ice could yield valuable information about heat transport in polar regions, where these dynamics may have significant implications for ice melt and climate feedback mechanisms.

This study employed only the MITgcm as a modeling framework. Future research could attempt to reproduce and validate the observed behaviors using alternative hydrostatic models, such as the Navy Coastal Ocean Model (NCOM) or Regional Ocean Modeling System (ROMS), to test the sensitivity of the results to numerical schemes and turbulence closures.

Other extensions might include varying the thermal anomaly of the filament while holding its width constant, to examine whether warmer filaments lead to stronger overturning and more vigorous eddy activity. This could provide a useful parallel to the present study, which primarily emphasized geometric rather than thermodynamic variation.

Ultimately, the consistent trends identified here suggest that warm filaments exhibit quantifiable, regular behaviors that depend on their initial geometry. With the impact that filaments and submesoscale eddies have on the global heat budget, transport of nutrients, and the energetics of the ocean, it is clear that a deeper understanding of their dynamics is critical for the development of more precise climate models and better prediction systems.

References

[AHC+04] Alistair Adcroft, Chris Hill, Jean-Michel Campin, John Marshall, and Patrick Heimbach. Overview of the formulation and numerics of the MIT GCM. In *Proceedings of the ECMWF seminar series on Numerical Methods, Recent developments in numerical methods for atmosphere and ocean modelling*, pages 139–149, 2004.

[AS07] Xosé Antón Alvarez-Salgado. Contribution of upwelling filaments to offshore carbon export in the subtropical Northeast Atlantic Ocean. *Limnology and Oceanography*, 52(3):1287–1292, 2007.

[FAW85] Pierre Flament, Laurence Armi, and Libe Washburn. The evolving structure of an upwelling filament. *Journal of Geophysical Research: Oceans*, 90(C6):11765–11778, 1985.

[GMM14] Jonathan Gula, M. Jeroen Molemaker, and James C. McWilliams. Submesoscale cold filaments in the Gulf Stream. *Journal of Physical Oceanography*, 44(10):2617 – 2643, 2014.

[HZFL+23] Seyed Mahmood Hamze-Ziabari, Mehrshad Foroughan, Ulrich Lemmin, Rafael Sebastian Reiss, and David Andrew Barry. The role of submesoscale filaments in restratification of the surface mixed layer and dissolved oxygen variability in large Lake Geneva: field evidence complemented by Lagrangian particle-tracking. *Frontiers in Marine Science*, 10:1200178, 2023.

[LK06] Guillaume Lapeyre and Patrice Klein. Impact of the small-scale elongated filaments on the oceanic vertical pump. *Journal of Marine Research*, 64(6):835–851, 2006.

[MCM09] JC McWilliams, François Colas, and MJ Molemaker. Cold filamentary intensification and oceanic surface convergence lines. *Geophysical research letters*, 36(18), 2009.

[McW17] James C McWilliams. Submesoscale surface fronts and filaments: Secondary circulation, buoyancy flux, and frontogenesis. *Journal of Fluid Mechanics*, 823:391–432, 2017.

[MIT24] MITgcm Group. *MITgcm User Manual*. Massachusetts Institute of Technology, 2024. https://mitgcm.readthedocs.io/en/latest/overview/overview.html.

[PHFK24] Anna Lo Piccolo, Christopher Horvat, and Baylor Fox-Kemper. Energetics and transfer of submesoscale brine-driven eddies at a sea ice edge. *Journal of Physical Oceanography*, 54(7):1489 – 1501, 2024.

[SW20] Qian Shi and Guihua Wang. Observed warm filaments from the Kuroshio associated with mesoscale eddies. *Remote Sensing*, 12(18):3090, 2020.

[SWK+18] Zhan Su, Jinbo Wang, Patrice Klein, Andrew F Thompson, and Dimitris Menemenlis. Ocean submesoscales as a key component of the global heat budget. *Nature communications*, 9(1):775, 2018.

[TT23] John R Taylor and Andrew F Thompson. Submesoscale dynamics in the upper ocean. *Annual Review of Fluid Mechanics*, 55(1):103–127, 2023.

[TWR+25] Hector S Torres, Alexander Wineteer, Ernesto Rodriguez, Patrice Klein, Andrew F Thompson, Dragana Perkovic-Martin, Jeroen Molemaker, Delphine Hypolite, Jörn Callies, J Thomas Farrar, et al. Submesoscale eddy contribution to ocean vertical heat flux diagnosed from airborne observations. *Geophysical Research Letters*, 52(2):e2024GL112278, 2025.

[YF24] Kai Yang and Andrew M Fischer. Assessing the impact of data-resolution on ocean frontal characteristics. *PFG–Journal of Photogrammetry, Remote Sensing and Geoinformation Science*, pages 1–17, 2024.

[ZLQ+23] Zhiwei Zhang, Yuelin Liu, Bo Qiu, Yiyong Luo, Wenju Cai, Qingguo Yuan, Yinxing Liu, Hong Zhang, Hailong Liu, Mingfang Miao, et al. Submesoscale inverse energy cascade enhances Southern Ocean eddy heat transport. *Nature Communications*, 14(1):1335, 2023.

Appendices

A Code

Python code used in analysis can be found on Github https://github.com/SpencerDFrancis/Submesoscale-Dynamics-of-Warm-Filaments

B Parameter Tables

cg2dMaxIters	1000
cg2dTargetResidual	1.E-13

Table 1: Elliptic solver parameters.

startTime	0.
nTimeSteps	21600
nTimeSteps	1440
deltaT	60
cAdjFreq	-1
abEps	0.1
pChkptFreq	8640000
chkptFreq	8640000
dumpFreq	8640000
dumpFreq	1
monitorFreq	8640000
monitorSelect	1
monitorFreq	1

Table 2: Time stepping parameters

usingCartesianGrid	TRUE
delR	10*20., 24., 29., 35., 42., 51., 61., 74.
	89., 107., 128., 155., 186., 224., 270., 325.
delR	100*4
delX	1600*100
delY	1000*100

Table 3: Gridding parameters

tRef	61*30., 29.5, 29., 28.5, 28., 27.5, 27., 26.5, 26., 25.5, 25., 24.5, 24., 23.5, 23., 22.5, 22., 21.5, 21., 20.5, 20., 19.5, 19., 18.5, 18., 17.5, 17., 16.5, 16., 15.5, 15., 14.5, 14., 13.5, 13., 12.5, 12., 11.5, 11., 10.5
viscAr	2.E-4
viscA4	12.E5
viscC2smag	3
no_slip_sides	FALSE
no_slip_bottom	TRUE
bottomDragLinear	1.E-3
bottomDragQuadratic	1.E-3
diffKrT	0.E-5
diffKrS	0.E-5
diffKrNrT	10*1.E-2, 30*2.E-5
diffKrNrS	10*1.E-2, 30*2.E-5
diffKhT	0.E3
diffKhS	0.E3
beta	0.E-11
f0	1.E-4
gravity	9.81
eosType	'LINEAR'
tAlpha	2.E-4
sBeta	0.E-4
rhoConst	1000
rhoNil	1000
rigidLid	FALSE
implicitFreeSurface	TRUE
implicitDiffusion	TRUE
tempAdvScheme	33
saltAdvScheme	33
staggerTimeStep	TRUE.
hMixCriteria	-0.1
hMixCriteria	1.5
readBinaryPrec	64
writeBinaryPrec	64

Table 4: Continuous equation parameters